actuators

MDPI

Article

A Backstepping Controller Based on a Model-Assisted Extended State Observer for a Slice Rotor Supported by Active Magnetic Bearings

Boyuan Xu *, Jin Zhou and Longxiang Xu

College of Mechanical and Electrical Engineering, Nanjing University of Aeronautics and Astronautics, Nanjing 210016, China
* Correspondence: xby@nuaa.edu.cn

Abstract: To improve the robustness of a slice rotor system supported by active magnetic bearings (AMBs), here, we propose a backstepping controller based on a model-assisted extended state observer (MESO-BC). Based on a generalized extended state observer (GESO), a model-assisted extended state observer is studied with consideration of the linear model of AMBs. The model-assisted extended state observer can estimate the unknown disturbances of the active magnetic bearing system, such as model inaccuracy and external disturbance, and is superior to the generalized extended state observer with respect to observation errors and the speed of convergence errors. In addition, it is compared with the backstepping controller based on a generalized extended state observer (GESO-BC) and conventional adaptive backstepping controller (ABC), and the simulation and experimental results verify the effectiveness of the proposed method. The experimental results demonstrate that the overshoot of the MESO-BC decrease by 5.94% and 13.2% as compared with the GESO-BC and ABC under the effect of pulse disturbance, respectively, and the rotor displacement of the MESO-BC reduce by 40.3% and 54.6% as compared with the GESO-BC and ABC under the effect of the sinusoidal disturbance, respectively.

Keywords: active magnetic bearings; slice rotor; backstepping control; extended state observer (ESO); disturbance rejection

Citation: Xu, B.; Zhou, J.; Xu, L. A Backstepping Controller Based on a Model-Assisted Extended State Observer for a Slice Rotor Supported by Active Magnetic Bearings. *Actuators* **2022**, *11*, 266. https://doi.org/10.3390/act11090266

Academic Editor: Zongli Lin

Received: 31 August 2022
Accepted: 9 September 2022
Published: 13 September 2022

1. Introduction

Active magnetic bearings (AMBs) have generally been applied in vacuum, pure, and high-speed industrial applications because of their non-mechanical contact, non-lubrication, and active control. The rotor can be categorized as a conventional rotor or a slice rotor according to its length. The length of a slice rotor is significantly smaller than its diameter, and usually only requires one radial magnetic bearing unit for stability. For industrial applications where space is a constraint, an AMB system with a slice rotor is generally applied, for example, in artificial hearts [1], optical scanning systems [2], and textiles [3].

In addition to determining the topological structure of a rotor, controlling the rotor position is one of the greatest challenges, which can determine the efficiency of the AMB system. However, magnetic bearings exhibit negative stiffness, indicating the inherent instability of magnetic bearing systems. Further, an AMB system is also susceptible to parameter variations and external disturbances that can cause the rotor to move from its equilibrium position. Therefore, the position of a rotor must be controlled by actively adjusting the control current of the coil and generating the corresponding electromagnetic force. As a result, several control strategies have been presented to limit the displacement of a rotor within a reasonable range. Proportional–integral–differential (PID) control is the most widely used strategy for position control due to its advantages in implementation and parameter tuning [4,5]. However, it is weakly robust to internal and external disturbances, such as system uncertainty or load vibrations [6]. To enhance the performance of the AMB

system with unknown dynamics, some advanced control strategies have been vigorously developed, such as H_∞ control [7], sliding-mode control [8], neural network control [9], observer-based control [10], predictive control [11], and backstepping control [12,13]. The backstepping control strategy has a favorable disturbance rejection capability for systems with external disturbances among these advanced control strategies. Moreover, the backstepping control strategy has a solid ability to adapt to uncertainties in system parameters, which can enhance transient performance when the system is disturbed [14]. Since it is usually difficult to determine the upper limits of disturbance, increasing the control voltage of controllers may contribute to better control performance; however, it is not an ideal solution.

A variety of observers have been proposed to estimate the unknown disturbance and to gain insight into unknown states. For the majority of observers, however, systematic model information is required. To overcome the dependence of observers on plant models, extended state observers have been studied and employed in AMB systems [15,16]. However, some of the above methods still use conventional PID controllers for position control, or the controllers are too complex for easy parameter adjustment.

In this paper, we present a backstepping controller based on a model-assisted extended state observer (MESO-BC) for a slice rotor supported by AMBs, which reduces control cost and increases robustness of the system to disturbance. The MESO-BC combines a backstepping control strategy with a model-assisted ESO that is used to estimate the state variables and lumped disturbances of the AMB system. The backstepping controller continuously updates its control law through the lumped disturbance estimated by the MESO in real time, thus, reducing the impact of uncertainties on the system. The novelty of the proposed method is that the model information about AMB dynamics is considered in the MESO design, which is used to estimate the lumped disturbance. The model information about AMB dynamics is added to the MESO design, which can reduce the workload of the MESO and can improve the disturbance estimation effect of the MESO. Therefore, the control performance of the MESO-BC is also improved and is superior to the backstepping controller based on a generalized extended state observer (GESO-BC).

This paper is organized as follows: The plant model of a slice rotor supported by AMBs is presented in Section 2; in Section 3, we demonstrate the design process of the backstepping controller and stability analysis using the Lyapunov theorem; in Section 4, we describe the GESO-BC, MESO-BC, and gain tuning strategy for the ESO; in Section 5, the simulation and experimental results on the AMB system demonstrate that the MESO-BC is superior to the GESO-BC and a conventional adaptive backstepping controller (ABC); in Section 6, we summarize the paper.

2. Model Description of the Slice Rotor Supported by AMBs

Figure 1 represents the employed three-dimensional structure of the slice rotor supported by AMBs. It contains a ring-shaped stator made of silicon lamination, which carries the magnetic flux. Eight coils are wound in the slot inside the ring-shaped stator. The dimensions and parameters of the AMB system are listed in Table 1.

2.1. Passive Stability of Axial and Tilting Directions

Since the rotor is slice-shaped (height < diameter) and has a height similar to the stator, the passive stability of the bearingless slice motor is also applied to the AMBs of the slice rotor [17]. According to the principle of slice-type rotors [18], the axial movements and deflection of the rotor are passively stabilized by reluctance forces. When the rotor generated an axial displacement (z-direction), the increased air gap between the rotor and stator resulted in a restoring reluctance force that eliminated the displacement (see Figure 2a). A similar torque was generated when the rotor was deflected around a radial axis (x- or y-axis), as shown in Figure 2b.

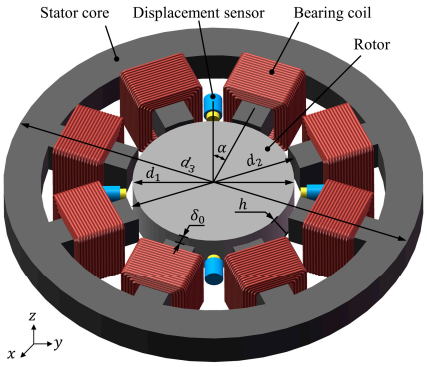

Figure 1. Topology of the slice rotor supported by one active magnetic bearing unit. x/y, radial direction; z, axial direction.

Table 1. The parameters of the AMB system.

Symbol	Parameter	Value	Unit
A_{mp}	Area of magnetic pole	56	mm^2
d_1	Rotor diameter	56.4	mm
d_2	Stator inner diameter	57.4	mm
d_3	Stator outer diameter	140	mm
h	Rotor height	13.2	mm
I_0	Bias current	1	A
k_a	Transfer function of the power amplifier	0.2	A/V
k_i	Current stiffness coefficient	3.7449	N/A
k_s	Transfer function of the displacement sensor	5	V/mm
k_x	Displacement stiffness coefficient	7489.72	N/m
m	Rotor mass	0.105	kg
N	Turns of single pole coil	120	—
α	Angle between the magnetic pole and the axis	22.5	deg
δ_0	Nominal air gap	0.5	mm

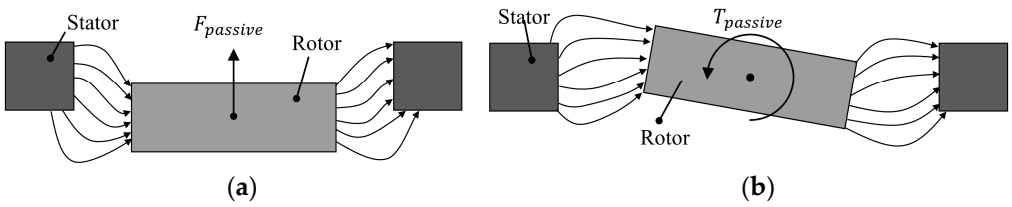

Figure 2. Passive stabilization: (**a**) Axial direction; (**b**) tilting directions.

2.2. Active Control of Radial Directions

Generally, the axial movements and deflections of the rotor are passively stabilized by reluctance forces. However, attracting force can pull the rotor even further away from equilibrium if the rotor produces radial displacements [19]. Thus, rotor movements must be controlled actively in radial directions. Without active-controlled bearing forces, the slice rotor cannot be stabilized in radial directions.

According to Newton's law, the plant model of radial magnetic bearings is obtained [20] as follows:

$$m\ddot{x} = k_x x + k_i i \tag{1}$$

where m represents rotor mass; x represents the rotor displacement in radial directions; i represents the control current; k_x and k_i represent the displacement stiffness coefficient and current stiffness coefficient of magnetic bearings, respectively, representing the linearized magnet force/displacement and force/current relationship at the equilibrium position. Valid in every degree of freedom, the displacement and current stiffness coefficient have

been proved through many years of practical experience to work extraordinarily well for a wide range of applications.

While Equation (1) only describes the fundamental behavior of AMBs under current control, it was a linear approximation of the actual relationship, which works in the proximity of the equilibrium position. However, many experimental results have shown that the linear relationship works successfully across a wide range. Furthermore, a more complex and nonlinear model should be considered only in limited circumstances, such as rotor-stator contact, extremely low bias currents, and flux saturation [21].

By applying Laplace transform to Equation (1), the magnetic bearing transfer function in radial directions can be derived, with rotor displacement $X(s)$ and control current $I(s)$ as output and input, respectively:

$$G(s) = \frac{X(s)}{I(s)} = \frac{k_i}{ms^2 - k_x} \tag{2}$$

We have k_i and k_x represented by:

$$k_i = \frac{\mu_0 N^2 A_{mp} I_0}{\delta_0^2} \cdot \cos\alpha \tag{3}$$

$$k_x = \frac{\mu_0 N^2 A_{mp} I_0^2}{\delta_0^3} \cdot \cos\alpha \tag{4}$$

where μ_0 represents the vacuum permeability, N represents the single-coil turns, A_{mp} represents the single magnetic pole area, α is the half-angle between two poles, I_0 is the bias current, and δ_0 is the nominal air gap.

The AMB system control loop with a linearized mechanical plant model, power amplifier, and displacement sensor is illustrated in Figure 3. The power amplifier and sensor can be modeled as linear transfer functions at low frequencies [15]. As exhibited in the control loop of the AMB system, Equation (2) can be rewritten with rotor displacement $X(s)$ and control voltage $U(s)$ as output and input, respectively:

$$G_P(s) = \frac{X(s)}{U(s)} = \frac{k_a k_i k_s}{ms^2 - k_x} \tag{5}$$

where k_a and k_s represent the transfer function of the power amplifier and sensors, respectively.

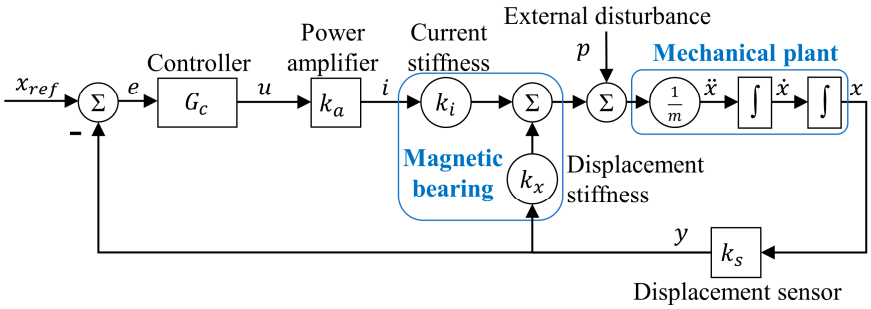

Figure 3. The AMB system control loop.

The rotor displacement $x(t)$ and velocity $\dot{x}(t)$ are assumed to be state variables. The input and output of the system are $u(t)$ and $y(t)$, respectively. Considering the external force p, the state-space description of the AMB system is represented by:

$$\begin{cases} \dot{x}_1 = x_2 \\ \dot{x}_2 = \frac{k_a k_i k_s}{m} u + \frac{k_x}{m} x_1 + \frac{p}{m} \\ y = x_1 \end{cases} \tag{6}$$

3. Backstepping Controller Design and Stability Proof

The AMB system is always subject to various uncertainties, including parameter variations, unknown dynamics, and external interferences, all of which have an adverse impact on the regular operation of the system. The slice rotor must remain near the equilibrium point when the AMB system is operating. Hence, the backstepping control method is adopted to generate appropriate bearing force to ensure that the rotor displacement remaines within acceptable boundaries.

The backstepping control method is the process of recursively determining control output step by step. First, a sophisticated system is split into several subsystems whose numbers do not exceed the order of the original system. Afterward, Lyapunov functions are constructed and the convergence of errors in each subsystem, by designing virtual control laws, is ensured. By recursion, the original system's output can be obtained. This procedure is described below.

Equation (6) indicates that AMBs are second-order systems. Nevertheless, the demand for precise AMB controllers has seen an increase with the advancement of model analysis. Consequently, in this study, an n-order backstepping controller is studied. The AMBs model presented in Equation (6) is rewritten in the form of a lower triangular system of n-order as follows:

$$\begin{cases} \dot{x}_i = x_{i+1} + F_i(x_1, \cdots, x_i),\ i = 1, \cdots, n-1 \\ \dot{x}_n = F_n(x) + bu + f, \\ y = x_1, \end{cases} \tag{7}$$

where $x_1, \cdots, x_n$ represent system state; $i \in \mathcal{N} \triangleq [1, \cdots, n]$ represent the order of the system; $f \in \mathbb{R}^p$ and $p \in \mathbb{N}$ are the constant and unknown, respectively, representing unmodeled disturbance; $F_i(\cdot)$ is the known linear or nonlinear function; u is control input; and b represents the known input coefficient.

The error variables of the system state are defined as:

$$\begin{cases} e_1 = x_{1d} - x_1, \\ e_i = x_{1d}^{(i-1)} + \varepsilon_{i-1} - x_i, \qquad i = 2, \cdots, n \end{cases} \tag{8}$$

where x_{1d} represents the desired displacement of the rotor, and virtual control laws can be designed as:

$$\begin{cases} \varepsilon_1 = k_1 e_1 - F_1(x), \\ \varepsilon_i = k_i e_i - F_i(x) + \dot{\varepsilon}_{i-1} + e_{i-1}, \qquad i = 2, \cdots, n-1 \end{cases} \tag{9}$$

To eliminate the unmodeled disturbance f, let the estimated value of f be $\hat{f}$. Note that disturbance f is constant. The error between f and $\hat{f}$ can be defined as:

$$\widetilde{f} = \hat{f} - f \tag{10}$$

Time derivative of $\widetilde{f}$ can be calculated as:

$$\dot{\widetilde{f}} = \dot{\hat{f}} \tag{11}$$

The design process of the n-order backstepping controller is described below, which can be divided into three steps. The final objective of this controller is to ensure that $x_1 \to x_{1d}$ as $t \to \infty$.

Step 1: The first Lyapunov function is designed as:

$$V_1 = \frac{1}{2} e_1^2 \tag{12}$$

Its time derivative can be denoted:

$$\dot{V}_1 = e_1(\dot{x}_{1d} - x_2) \tag{13}$$

Equations (8) and (9) are substituted into (13):

$$\dot{V}_1 = -k_1 e_1^2 + e_1 e_2 \tag{14}$$

If the error variable $e_2 = 0$, e_1 will converge asymptotically according to the Lyapunov theorem.

Step 2: From the defined error variables, the corresponding Lyapunov function for e_i $(i = 2, \cdots, n-1)$ can be expressed as:

$$V_i = V_{i-1} + \frac{1}{2} e_i^2 \tag{15}$$

Its time derivative can be calculated as:

$$\dot{V}_i = \dot{V}_{i-1} + e_i \left[x_{1d}^{(i)} + \dot{\varepsilon}_{i-1} - \dot{x}_i \right] \tag{16}$$

From Equation (7) and the designed virtual control law, Equation (16) can be rewritten as:

$$\begin{aligned} \dot{V}_i &= \dot{V}_{i-1} - k_i e_i^2 + e_i e_{i+1} - e_i e_{i-1} \\ &= -\sum_{j=1}^{i-1} k_j e_j^2 + e_{i-1} e_i - k_i e_i^2 + e_i e_{i+1} - e_i e_{i-1} \\ &= -\sum_{j=1}^{i} k_j e_j^2 + e_i e_{i+1} \end{aligned} \tag{17}$$

If $e_{i+1} = 0$, the error variables e_i $(i = 1, \cdots, n-1)$ will converge asymptotically.

Step 3: The final Lyapunov function can be constructed as:

$$V_n = V_{n-1} + \frac{1}{2} e_n^2 + \frac{1}{2} \rho \tilde{f}^2 \tag{18}$$

where $\rho = e_n / \dot{\hat{f}} > 0$ represents the compensation coefficient. The corresponding derivative of V_n can be calculated as:

$$\begin{aligned} \dot{V}_n &= \dot{V}_{n-1} + e_n \dot{e}_n + \rho \tilde{f} \dot{\tilde{f}} \\ &= \dot{V}_{n-1} + e_n \left[x_{1d}^{(n)} + \dot{\varepsilon}_{n-1} - F_n(x) - bu - f \right] + \rho \tilde{f} \dot{\tilde{f}} \\ &= -\sum_{j=1}^{n-1} k_j e_j^2 + e_n [e_{n-1} + x_{1d}^{(n)} + \dot{\varepsilon}_{n-1} - F_n(x) - bu - f] + \rho \tilde{f} \dot{\tilde{f}} \end{aligned} \tag{19}$$

The control law u needing to be designed appears and could be designed as:

$$u = \frac{1}{b} \left[e_{n-1} + x_{1d}^{(n)} + \dot{\varepsilon}_{n-1} - F_n(x) - \hat{f} + k_n e_n \right] \tag{20}$$

where $\hat{f}$ is estimated in real time by the ESO. Equation (20) is substituted into (19):

$$\begin{aligned} \dot{V}_n &= -\sum_{j=1}^{n-1} k_j e_j^2 - k_n e_n^2 + e_n \left(f - \hat{f} \right) + \rho \tilde{f} \dot{\tilde{f}} \\ &= -\sum_{j=1}^{n} k_j e_j^2 \leq 0 \end{aligned} \tag{21}$$

According to the Lyapunov-like lemma, the error variables e_i $(i = 1, \cdots, n)$ are convergent asymptotically, meaning that the rotor can track the desired displacement.

4. ESO-Based Backstepping Controller Design

4.1. Extended State Observer

The backstepping control strategy has certain robustness to modeling inaccuracy and external disturbance [21]. Nevertheless, a larger control gain is required for the backstepping control strategy to be robust against the fast-changing disturbances of unknown form or more significant disturbances, which can lead to a larger control voltage and undesirable chattering problem. Thus, in this section, we aim at exploring the application of the ESO to observe and compensate for system disturbance during the control process.

An ESO was proposed as the core of active disturbance rejection control [22,23]. The ESO begins by borrowing the idea of a state observer, expanding the disturbance possibly affecting controller outputs into a new system state variable, and then reconstructing all the states of the original state variable and disturbance using system inputs and outputs. The ESO includes both linear and nonlinear ESOs. The nonlinear ESO uses nonlinear functions containing many parameters, and tuning can be quite challenging. Accordingly, the linear ESO is considered in this study to observe disturbance.

Consideration is given to a second-order nonlinear system with single-input and -output u and y, respectively:

$$\begin{cases} \dot{x}_1 = x_2 \\ \dot{x}_2 = f(x_1, x_2, t, \omega(t)) + bu \\ y = x_1 \end{cases} \tag{22}$$

where b is the known input coefficient, ω is the external disturbance. Here, $f(x_1, x_2, t, \omega(t))$ is simply denoted as f_{ld}, representing the lumped disturbance. The only information given for this plant is the system order and parameter b, which indicates that the ESO is not dependent on accurate plant models. To this end, f_{ld} is assumed to be differentiable and $h = \dot{f}_{ld}$. Equation (22) can be augmented as:

$$\begin{cases} \dot{x}_1 = x_2 \\ \dot{x}_2 = x_3 + bu \\ \dot{x}_3 = h = \dot{f}_{ld} \\ y = x_1 \end{cases} \tag{23}$$

To estimate the system states, the following linear ESO with inputs u and y is used:

$$\begin{cases} \dot{\hat{x}}_1 = \hat{x}_2 - l_1(\hat{x}_1 - x_1) \\ \dot{\hat{x}}_2 = \hat{x}_3 - l_2(\hat{x}_1 - x_1) + bu \\ \dot{\hat{x}}_3 = -l_3(\hat{x}_1 - x_1) \end{cases} \tag{24}$$

where l_1, l_2, and l_3 are observer gains needing to be designed.

The error system of Equations (23) and (24) is obtained as:

$$\begin{cases} \dot{e}_1 = e_2 - l_1 e_1 \\ \dot{e}_2 = e_3 - l_2 e_1 \\ \dot{e}_3 = -l_3 e_1 - \dot{f}_{ld} \end{cases} \tag{25}$$

where $e_i = \hat{x}_i - x_i$, and $i = 1, 2, 3$ are estimation errors. The errors are convergence to zero for well-tuned l_1, l_2, and l_3. The control law is updated to:

$$u = \frac{u_0 - \hat{f}_{ld}}{b} \tag{26}$$

where u_0 is the feedback control law of errors, reducing Equation (22) to a cascade integral form plant:

$$\dot{x}_2 \approx u_0 \tag{27}$$

which can be easily controlled utilizing state feedback as compared with the original system. The stability analysis of the ESO is given in [24]. In this paper, the ESO using only the system order and parameter b is denoted as the GESO.

4.2. The GESO-BC Design

The GESO required no accurate plant information for its design. Thus, suppose that only the system order and input coefficient b can be obtained. The state-space description of Equation (6) can be augmented as:

$$\begin{cases} \dot{x}_1 = x_2 \\ \dot{x}_2 = x_3 + \frac{k_a k_i k_s}{m} u \\ \dot{x}_3 = \dot{f}_{ld} \\ y = x_1 \end{cases} \tag{28}$$

where $x_3 = f_{ld}$ represents the lumped disturbance. The augmented state-space description of the system is:

$$\begin{cases} \dot{\boldsymbol{x}} = \boldsymbol{A}\boldsymbol{x} + \boldsymbol{B}\boldsymbol{u} + \boldsymbol{E}\boldsymbol{h} \\ \boldsymbol{y} = \boldsymbol{C}\boldsymbol{x} \end{cases} \tag{29}$$

with $\boldsymbol{A} = \begin{bmatrix} 0 & 1 & 0 \\ 0 & 0 & 1 \\ 0 & 0 & 0 \end{bmatrix}$, $\boldsymbol{B} = \begin{bmatrix} 0 \\ \frac{k_a k_i k_s}{m} \\ 0 \end{bmatrix}$, $\boldsymbol{C} = \begin{bmatrix} 1 & 0 & 0 \end{bmatrix}$, $\boldsymbol{E} = \begin{bmatrix} 0 \\ 0 \\ 1 \end{bmatrix}$ and $\boldsymbol{h} = \begin{bmatrix} \dot{f}_{ld} \end{bmatrix}$.

According to the form of the general Luenberger observer,

$$\begin{cases} \dot{\hat{\boldsymbol{x}}} = \boldsymbol{A}\hat{\boldsymbol{x}} + \boldsymbol{B}\boldsymbol{u} + \boldsymbol{L}(\boldsymbol{y} - \hat{\boldsymbol{y}}) \\ \hat{\boldsymbol{y}} = \boldsymbol{C}\hat{\boldsymbol{x}} \end{cases} \tag{30}$$

bring $\hat{\boldsymbol{y}} = \boldsymbol{C}\hat{\boldsymbol{x}}$ into $\dot{\hat{\boldsymbol{x}}}$, and Equation (30) is rewritten as follows with u and y as inputs:

$$\begin{cases} \dot{\hat{\boldsymbol{x}}} = \overline{\boldsymbol{A}}\hat{\boldsymbol{x}} + \overline{\boldsymbol{B}}\overline{\boldsymbol{u}} \\ \hat{\boldsymbol{y}} = \overline{\boldsymbol{C}}\hat{\boldsymbol{x}} + \overline{\boldsymbol{D}}\overline{\boldsymbol{u}} \end{cases} \tag{31}$$

with $\overline{\boldsymbol{A}} = \begin{bmatrix} -l_1 & 1 & 0 \\ -l_2 & 0 & 1 \\ -l_3 & 0 & 0 \end{bmatrix}$, $\overline{\boldsymbol{B}} = \begin{bmatrix} 0 & l_1 \\ \frac{k_a k_i k_s}{m} & l_2 \\ 0 & l_3 \end{bmatrix}$, $\overline{\boldsymbol{u}} = \begin{bmatrix} u \\ y \end{bmatrix}$, $\overline{\boldsymbol{C}} = \begin{bmatrix} 1 & 0 & 0 \\ 0 & 1 & 0 \\ 0 & 0 & 1 \end{bmatrix}$, $\overline{\boldsymbol{D}} = \begin{bmatrix} 0 & 0 \\ 0 & 0 \\ 0 & 0 \end{bmatrix}$.

The GESO can work more efficiently by configuring observer gains more conveniently. Therefore, all the eigenvalues of $\overline{A}$ are placed at $-\omega_o$, representing observer bandwidth [25]. The gain of the GESO can be obtained:

$$\boldsymbol{L} = \begin{bmatrix} l_1 & l_2 & l_3 \end{bmatrix} = \begin{bmatrix} 3\omega_o & 3\omega_o^2 & \omega_o^3 \end{bmatrix} \tag{32}$$

From Equation (26), the GESO estimated the lumped disturbance $\hat{f}_{ld}$ for updating the control law, and a new control law of the GESO-BC is obtained:

$$u' = \frac{m}{k_i k_s k_a}\left(e_1 + \ddot{x}_{1d} + k_1 \dot{e}_1 + k_2 e_2 - \hat{f}_{ld}\right) \tag{33}$$

4.3. The MESO-BC Design

As mentioned previously, the GESO is not reliant on accurate plant models. However, plant information is available, which can be incorporated into the ESO design, reducing its bandwidth and sensitivity to noise [26,27]. The internal dynamic of the AMB system f_{in} is

completely known, that is, $f_{in} = \frac{k_x}{m} x_1$ is given in Equation (6). Then, the new augmented system can be obtained:

$$\begin{cases} \dot{x}_1 = x_2 \\ \dot{x}_2 = x_3 + \frac{k_a k_i k_s}{m} u \\ \dot{x}_3 = \dot{f}_{ld} = \dot{f}_{ex} + \dot{f}_{in} \\ y = x_1 \end{cases} \tag{34}$$

where f_{ex} is the external disturbance other than f_{in}. The state-space description can be rewritten as:

$$\begin{cases} \dot{\boldsymbol{x}} = \boldsymbol{A}'\boldsymbol{x} + \boldsymbol{B}\boldsymbol{u} + \boldsymbol{E}\boldsymbol{h}' \\ \boldsymbol{y} = \boldsymbol{C}\boldsymbol{x} \end{cases} \tag{35}$$

with $\boldsymbol{A}' = \begin{bmatrix} 0 & 1 & 0 \\ 0 & 0 & 1 \\ 0 & \frac{k_x}{m} & 0 \end{bmatrix}$, $\boldsymbol{h}' = [\dot{f}_{ex}]$.

The corresponding MESO can be obtained as follows with u and y as inputs:

$$\begin{gathered} \begin{bmatrix} \dot{\hat{x}}_1 \\ \dot{\hat{x}}_2 \\ \dot{\hat{x}}_3 \end{bmatrix} = \begin{bmatrix} -l_1' & 1 & 0 \\ -l_2' & 0 & 1 \\ -l_3' & \frac{k_x}{m} & 0 \end{bmatrix} \begin{bmatrix} \hat{x}_1 \\ \hat{x}_2 \\ \hat{x}_3 \end{bmatrix} + \begin{bmatrix} 0 & l_1' \\ \frac{k_a k_i k_s}{m} & l_2' \\ 0 & l_3' \end{bmatrix} \begin{bmatrix} u \\ y \end{bmatrix} + \begin{bmatrix} 0 \\ 0 \\ 1 \end{bmatrix} [\dot{f}_{ex}] \\ \hat{\boldsymbol{y}} = \begin{bmatrix} 1 & 0 & 0 \\ 0 & 1 & 0 \\ 0 & 0 & 1 \end{bmatrix} \begin{bmatrix} \hat{x}_1 \\ \hat{x}_2 \\ \hat{x}_3 \end{bmatrix} + \begin{bmatrix} 0 & 0 \\ 0 & 0 \\ 0 & 0 \end{bmatrix} \begin{bmatrix} u \\ y \end{bmatrix} \end{gathered} \tag{36}$$

All the eigenvalues of $\begin{bmatrix} -l_1' & 1 & 0 \\ -l_2' & 0 & 1 \\ -l_3' & \frac{k_x}{m} & 0 \end{bmatrix}$ are placed at $-\omega_o$, and the MESO gain was obtained as follows:

$$\boldsymbol{L}' = \begin{bmatrix} l_1' & l_2' & l_3' \end{bmatrix} = \begin{bmatrix} 3\omega_o & 3\omega_o^2 + \frac{k_x}{m} & \omega_o^3 + \frac{3\omega_o k_x}{m} \end{bmatrix} \tag{37}$$

According to Equation (37), the MESO gain is higher than that of the GESO (see Equation (32)) at the same bandwidth ω_o. The corresponding control law of the MESO-BC can be formulated as follows by considering the estimated disturbances f_{in} and f_{ex}:

$$u'' = \frac{m}{k_i k_s k_a} \left(e_1 + \ddot{x}_{1d} + k_1 \dot{e}_1 + k_2 e_2 - \hat{f}_{in} - \hat{f}_{ex} \right) \tag{38}$$

5. Simulation and Experimental Verification

In this section, simulation studies and experimental tests applying the MESO-BC, the GESO-BC, and the existing adaptive backstepping controller based on the quadratic Lyapunov function [28] to the AMB system were performed to verify the effectiveness of the proposed controller. The dimensions and parameters of the employed AMB system are listed in Table 1.

5.1. Simulations Results

5.1.1. Simulations of Floating Performance Contrast

The rotor stops randomly within the air gap when the AMB system is out of operation, and returns to its equilibrium position if the system is restarted. The starting and equilibrium positions of the rotor are assumed to be (−0.5, 0 mm) and (0, 0 mm), respectively. Additionally, the controller parameters k_1 and k_2 are chosen as 200 and 400, respectively, to ensure fairness. The adaptive coefficient k_e of the ABC is chosen as 0.25, and the bandwidth ω_o of the GESO and the MESO is selected as 2000.

Figure 4 illustrates the simulation results for rotor floating, and Figure 5 shows the observation errors of the GESO and the MESO. In Figure 4, the maximum overshoot

values of the ABC, GESO-BC, and MESO-BC are 0.1124 mm, 0.0971 mm, and 0.0949 mm, respectively. The settling times of the ABC, GESO-BC, and MESO-BC are 0.0350 s, 0.0309 s, and 0.0305 s, respectively. As presented in Figure 5, both the observation errors of the GESO and MESO converged to zero. However, the MESO has more minor observation errors and faster errors convergence.

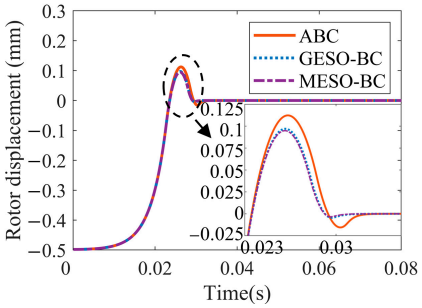

Figure 4. Floating performance simulation results.

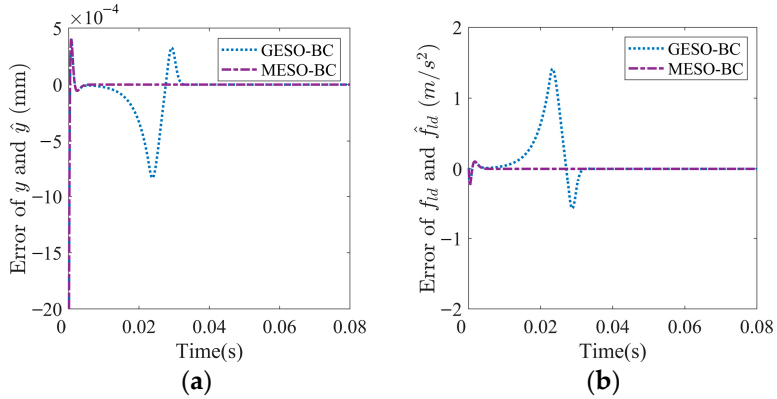

Figure 5. ESO estimation errors: (**a**) Estimation error of y and $\hat{y}$; (**b**) estimation error of f_{ld} and $\hat{f}_{ld}$.

5.1.2. Simulations Contrast of Robustness to External Disturbances

The external pulse and sinusoidal disturbances are injected into the AMB system. Figure 6 shows the response waveforms with a 3 N external pulse disturbance, a period of 1 s, and a pulse width of 1%. Figure 7 displays the estimation errors for the GESO and MESO. As illustrated in Figure 6, the maximum overshoot values of the ABC, GESO-BC, and MESO-BC are 0.1181 mm, 0.0975 mm, and 0.0731 mm, respectively. The adjustment time for the GESO-BC and MESO-BC is approximately 0.05 s, while that for the ABC is longer and exceeds 0.1 s. As shown in Figure 7, the MESO exhibits more minor estimation errors than the GESO for the same bandwidth, and observation errors can converge in a shorter period.

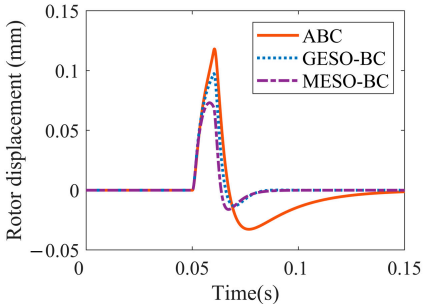

Figure 6. Response waveforms under 3 N pulse disturbance simulations.

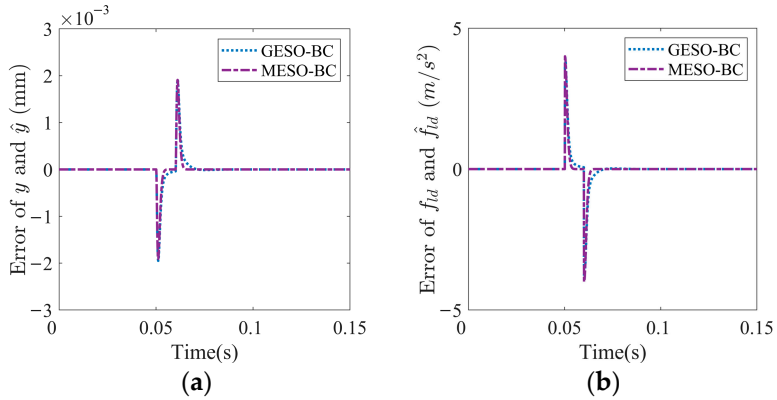

Figure 7. ESO estimation errors: (**a**) Estimation error of y and $\hat{y}$; (**b**) estimation error of f_{ld} and $\hat{f}_{ld}$.

The system is subjected to a sinusoidal disturbance with an amplitude of 6 N at a frequency of 200 Hz. The response waveforms and observation errors are shown in Figures 8 and 9. Figure 8 indicates the peak-to-peak values for the ABC, GESO-BC, and MESO-BC are 0.116 mm, 0.100 mm, and 0.095 mm, respectively. Figure 9 shows that the GESO has greater observation errors than the MESO.

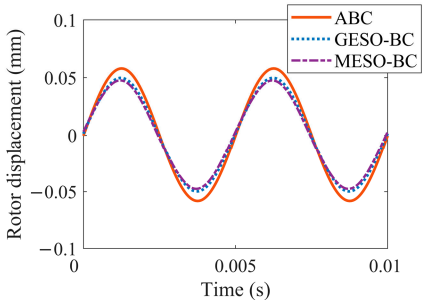

Figure 8. Response waveforms under 6 N sinusoidal disturbance simulations.

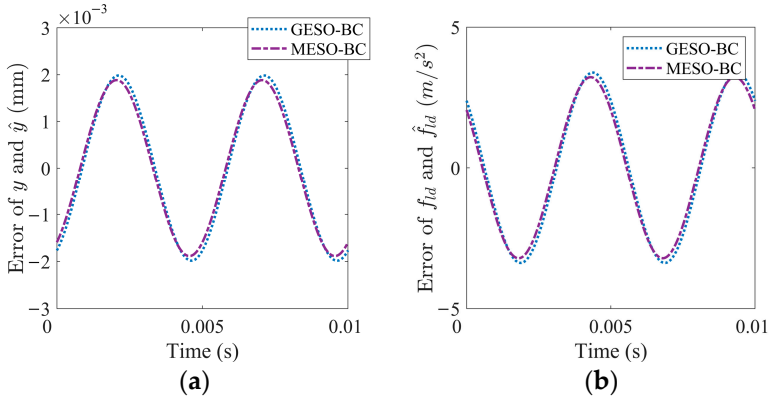

Figure 9. ESO estimation errors: (**a**) Estimation error of y and $\hat{y}$; (**b**) estimation error of f_{ld} and $\hat{f}_{ld}$.

Based on the above simulation results, ESO-based backstepping controllers are superior to ABC concerning both overshoot and stabilization time. Moreover, a comparison of the MESO-BC and GESO-BC shows that the MESO model information-assisted design has better observation results and faster convergence of observation errors than the GESO in the case of the same bandwidth. Observation errors can be reduced by increasing the bandwidth of the ESO. However, the bandwidth is limited by the sampling noise of the system. Increasing the bandwidth of the ESO will increase the sensitivity of the system to noise. Therefore, the ESO bandwidth should be determined by balancing the size of observation errors and the sensitivity of the system to measurement noise.

5.2. Experimental Setup

In this paper, a slice rotor supported by AMBs was constructed as a testing platform to verify the feasibility and performance of a MESO-BC. Figure 10 presents the annotated photograph of the test platform, consisting primarily of a slice rotor supported by AMBs, the motor, the power amplifier, the digital control system, and the power supply system, where the motor and rotor are connected by a flexible coupling. Flexible couplings serve only to direct the rotation of the rotor without affecting the axial displacement of the rotor. Moreover, rotor displacement is measured by two sets of differential displacement sensors in both radial directions, and the sampling frequency is 10 kHz.

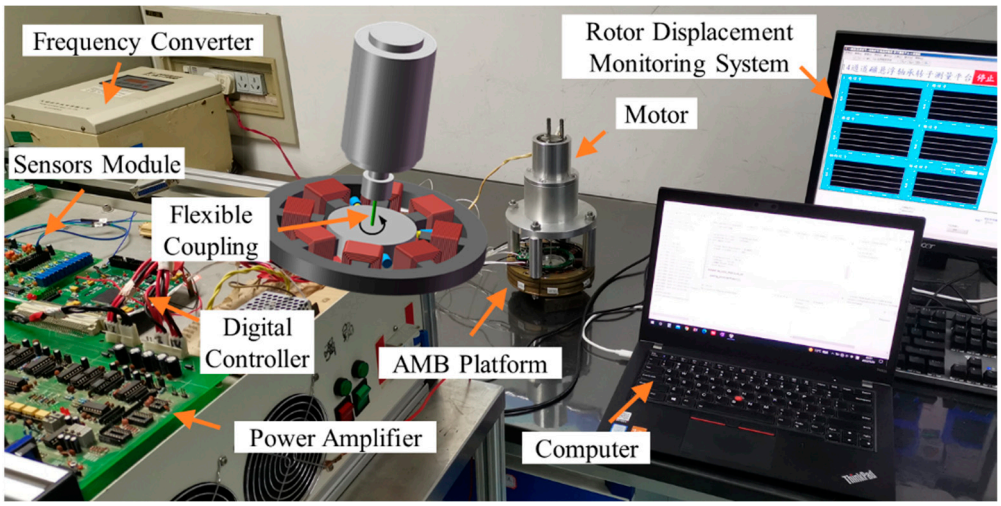

Figure 10. Photograph of the constructed AMB platform.

The experimental research includes floating experiments, pulse and sinusoidal disturbance rejection experiments, and rotational experiments. A GESO-BC and a conventional ABC are also used for comparison.

5.3. Experimental Results

5.3.1. Experimental Floating Performance

Figure 11 shows the results of the floating experiment in the x-direction of the rotor, which has been enlarged for a more detailed view. The maximum overshoot values of the ABC, GESO-BC, and MESO-BC are 0.178 mm, 0.138 mm and 0.122 mm, respectively. The settling time for the GESO-BC and MESO-BC is approximately 0.025 s, which is significantly faster than 0.05 s for the ABC.

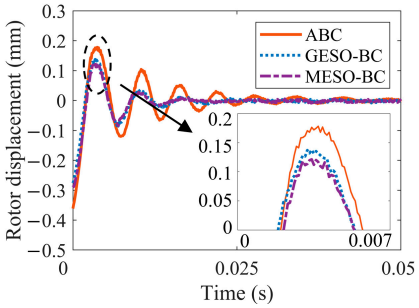

Figure 11. Floating performance experimental results.

5.3.2. Experimental Contrast of Robustness to External Disturbances

A pulse disturbance of 3 N and a sinusoidal disturbance of 6 N with a frequency of 200 Hz were injected into the AMB system in the x-direction to demonstrate the robustness to the external disturbance of the MESO-BC.

Figure 12 presents the rejection results of 3 N pulse disturbance. Figure 12a shows the rotor displacement, and Figure 12b shows the control voltage. In Figure 12a, it is evident that the rotor controlled by the GESO-BC and MESO-BC demonstrated more rapid stability. By comparing the GESO-BC and MESO-BC, it can be found that the rotor displacement under the control of the MESO-BC is more minor than that of the GESO-BC. For quantitative comparison, the $\mathcal{L}^2$ norm of the rotor displacement tracking error e and control output voltage u are calculated, denoted as $||e||_2$ and $||u||_2$, respectively. The $||e||_2$ values for the ABC, GESO-BC, and MESO-BC are 0.9113, 0.8400, and 0.7901, respectively, indicating that the MESO-BC has the smallest tracking error. Moreover, the ABC, GESO-BC, and MESO-BC have $||u||_2$ values of 25.9171, 18.3519, and 17.3877, respectively, implying that the MESO-BC has the lowest control cost.

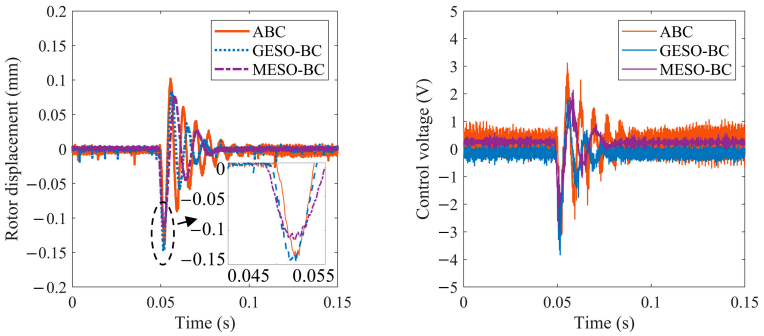

Figure 12. Response waveforms under 3 N pulse disturbance experiments: (**a**) Rotor displacement; (**b**) control voltage.

The rejection waveforms of 6 N sinusoidal disturbance are shown in Figure 13. As illustrated in Figure 13a, the peak-to-peak displacement values of the slice rotor controlled by the ABC, GESO-BC, and MESO-BC are approximately 0.207 mm, 0.159 mm, and 0.096 mm, respectively. The ABC, GESO-BC, and MESO-BC have $||e||_2$ values of 1.0256, 0.7807, and 0.4657, respectively, implying that the displacement tracking performance of the MESO-BC is superior to that of the GESO-BC and ABC. The $||u||_2$ values for the ABC, GESO-BC, and MESO-BC are 24.5332, 18.0029, and 15.3364, respectively, suggesting that the MESO-BC has a lower control cost than the GESO-BC and ABC, and is more energy-efficient.

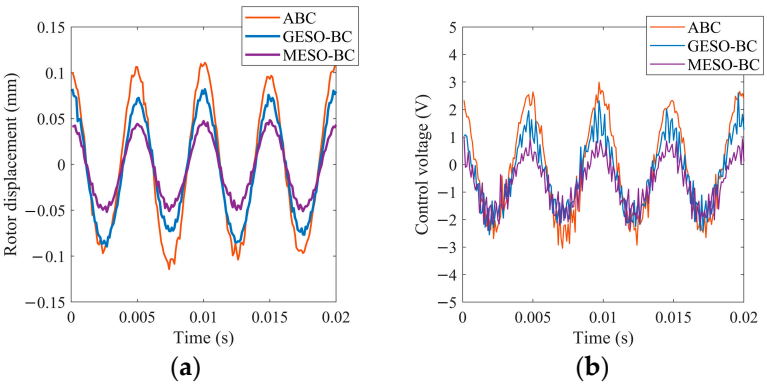

Figure 13. Response waveforms under 6 N sinusoidal disturbance experiments: (**a**) Rotor displacement; (**b**) control voltage.

The GESO-BC is compared with the MESO-BC to find that the MESO designed with the aid of plant information can obtain more accurate disturbance observations.

5.3.3. Experimental Rotation Performance

To evaluate the performance of each controller, the rotor was accelerated to a rotational speed of 12,000 rpm (200 Hz) and stabilized at that speed. Figure 14 illustrates the rotor displacement. In Figure 14, the maximum rotor displacements during acceleration for the ABC, GESO-BC, and MESO-BC are 0.0933 mm, 0.0651 mm, and 0.0597 mm, respectively. For quantitative comparison, the ABC, GESO-BC, and MESO-BC have $||e||_2$ values of 20.6672, 20.2093, and 19.4420, respectively. Furthermore, the $||u||_2$ values for the ABC, GESO-BC, and MESO-BC are 496.9778, 485.7276, and 475.5005, respectively. The experimental results show that the MESO-BC has displacement tracking performance superior to the GESO-BC and ABC, and lower control cost.

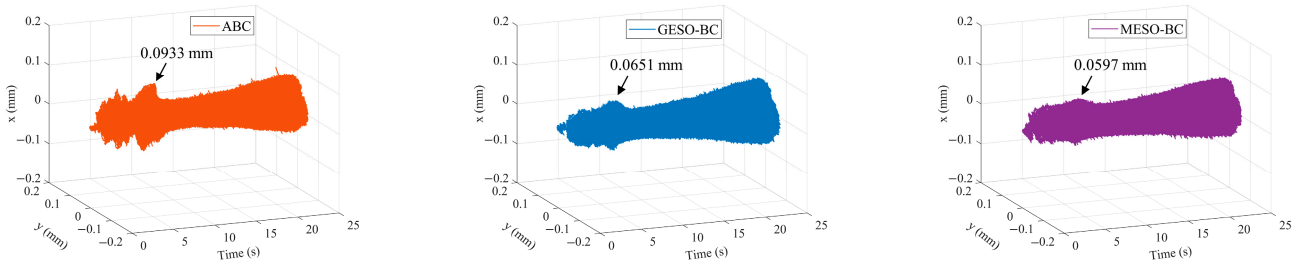

(**a**) (**b**) (**c**)

Figure 14. Rotor displacement from standstill to 12,000 rpm (200 Hz) accelerated rotation experiments: (**a**) ABC; (**b**) GESO-BC; (**c**) MESO-BC.

According to the above experimental results, the ESO has the capability of estimating the lumped disturbance of the AMB system and compensating for it in the control process. Furthermore, the MESO has smaller observation errors and faster convergence of observation errors than the GESO for the same bandwidth. The reason is that the MESO incorporated known model information into its design. Therefore, the MESO-BC provided better control performance.

6. Conclusions

A backstepping controller based on a MESO is proposed to improve the displacement tracking performance and robustness for a slice rotor supported by AMBs. First, a backstepping controller for the AMB system is developed. Then, a MESO is designed with consideration of the model information about AMB dynamics, and then is used to estimate the lumped disturbance of the AMB system. The tuning method of the MESO bandwidth is also given. The control law of the backstepping controller is updated online based on the lumped disturbance estimated by the MESO, thus, reducing the influence of uncertainties on the system.

To validate the effectiveness of the MESO-BC, simulations and experiments are conducted, and the MESO-BC is compared with a GESO-BC and an ABC. The simulation results show that the MESO has more minor observation errors and faster convergence of observation errors than the GESO in the case of the same bandwidth because the model information about AMB dynamics is considered in the MESO design, which can reduce the workload of the MESO. The experimental results demonstrate that the slice rotor under the control of the MESO-BC has minor displacement tracking error, stronger robustness to the lumped disturbance, and lower control cost than under the control of the GESO-BC and the ABC. Therefore, the robustness and displacement tracing performances of the system of a slice rotor supported by AMBs are improved.

Author Contributions: Conceptualization, methodology, validation, writing—original draft preparation, B.X.; writing—review and editing, supervision, J.Z. and L.X. All authors have read and agreed to the published version of the manuscript.

Funding: This research was funded by the Key R&D program of Jiangsu Province (grant no. BE2019122), and the Six Talent Peaks Project in Jiangsu Province (grant no. JNHB-041).

Conflicts of Interest: The authors declare no conflict of interest.

References

1. Asama, J.; Fukao, T.; Chiba, A.; Rahman, A.; Oiwa, T. A design consideration of a novel bearingless disk motor for artificial hearts. In Proceedings of the 2009 IEEE Energy Conversion Congress and Exposition, San Jose, CA, USA, 20–24 September 2009; pp. 1693–1699.
2. Puentener, P.; Schuck, M.; Steinert, D.; Nussbaumer, T.; Kolar, J.W. A 150,000-r/min Bearingless Slice Motor. *IEEE/ASME Trans. Mechatron.* **2018**, *23*, 2963–2967. [CrossRef]
3. Silber, S.; Sloupensky, J.; Dirnberger, P.; Moravec, M.; Amrhein, W.; Reisinger, M. High-Speed Drive for Textile Rotor Spinning Applications. *IEEE Trans. Ind. Electron.* **2014**, *61*, 2990–2997. [CrossRef]
4. Jeon, H.-W.; Lee, C.-W. Proportional-integral-derivative control of rigid rotor-active magnetic bearing system via eigenvalue assignment for decoupled translational and conical modes. *J. Vib. Control.* **2015**, *21*, 2372–2393. [CrossRef]
5. Sun, J.; Zhou, H.; Ma, X.; Ju, Z. Study on PID tuning strategy based on dynamic stiffness for radial active magnetic bearing. *ISA Trans.* **2018**, *80*, 458–474. [CrossRef] [PubMed]
6. Breńkacz, Ł.; Witanowski, Ł.; Drosińska-Komor, M.; Szewczuk-Krypa, N. Research and applications of active bearings: A state-of-the-art review. *Mech. Syst. Signal Process.* **2021**, *151*, 107423. [CrossRef]
7. Balini, H.M.N.K.; Scherer, C.W.; Witte, J. Performance Enhancement for AMB Systems Using Unstable H_∞ Controllers. *IEEE Trans. Control. Syst. Technol.* **2011**, *19*, 1479–1492. [CrossRef]
8. Abooee, A.; Arefi, M.M. Robust finite-time stabilizers for five-degree-of-freedom active magnetic bearing system. *J. Frankl. Inst.* **2019**, *356*, 80–102. [CrossRef]
9. Sun, X.; Su, B.; Chen, L.; Yang, Z.; Xu, X.; Shi, Z. Precise control of a four degree-of-freedom permanent magnet biased active magnetic bearing system in a magnetically suspended direct-driven spindle using neural network inverse scheme. *Mech. Syst. Signal Process.* **2017**, *88*, 36–48. [CrossRef]
10. Mystkowski, A.; Kierdelewicz, A.; Kotta, Ü.; Kaparin, V. Experimental validation of the Newton observer for a nonlinear flux-controlled AMB system operated with zero-bias flux. *Int. J. Control.* **2020**, *93*, 2257–2266. [CrossRef]
11. Li, D.; Cao, H.; Zhang, X.; Chen, X.; Yan, R. Model predictive control based active chatter control in milling process. *Mech. Syst. Signal Process.* **2019**, *128*, 266–281. [CrossRef]
12. Wu, M.; Zhu, H. Backstepping control of three-pole radial hybrid magnetic bearing. *IET Electr. Power Appl.* **2020**, *14*, 1405–1411. [CrossRef]
13. Yang, D.; Gao, X.; Cui, E.; Ma, Z. State-Constraints Adaptive Backstepping Control for Active Magnetic Bearings with Parameters Nonstationarities and Uncertainties. *IEEE Trans. Ind. Electron.* **2021**, *68*, 9822–9831. [CrossRef]
14. Pavlichkov, S.S.; Dashkovskiy, S.N.; Pang, C.K. Uniform Stabilization of Nonlinear Systems with Arbitrary Switchings and Dynamic Uncertainties. *IEEE Trans. Autom. Control.* **2017**, *62*, 2207–2222. [CrossRef]
15. Jin, C.W.; Guo, K.X.; Xu, Y.P.; Cui, H.B.; Xu, L.X. Design of Magnetic Bearing Control System Based on Active Disturbance Rejection Theory. J. Vib. Acoust.-Trans. *ASME* **2019**, *141*, 011009.
16. Li, K.; Peng, C.; Deng, Z.; Huang, W.; Zhang, Z. Field dynamic balancing for active magnetic bearings supporting rigid rotor shaft based on extended state observer. *Mech. Syst. Signal Process.* **2021**, *158*, 107801. [CrossRef]
17. Schoeb, R.; Barletta, N. Principle and Application of a Bearingless Slice Motor. *JSME Int. J. Ser. C Mech. Syst. Mach. Elem. Manuf.* **1997**, *40*, 593–598.
18. Nussbaumer, T.; Karutz, P.; Zurcher, F.; Kolar, J.W. Magnetically Levitated Slice Motors—An Overview. *IEEE Trans. Ind. Appl.* **2011**, *47*, 754–766. [CrossRef]
19. Steinert, D.; Nussbaumer, T.; Kolar, J.W. Concept of a 150 krpm bearingless slotless disc drive with combined windings. In Proceedings of the 2013 International Electric Machines & Drives Conference, Chicago, IL, USA, 12–15 May 2013; pp. 311–318.
20. Schweitzer, G.; Maslen, E.H. *Magnetic Bearings: Theory, Design, and Application to Rotating Machinery*; Springer: Berlin/Heidelberg, Germany, 2009.
21. Yousefizadeh, S.; Bendtsen, J.D.; Vafamand, N.; Khooban, M.H.; Blaabjerg, F.; Dragičević, T. Tracking Control for a DC Microgrid Feeding Uncertain Loads in More Electric Aircraft: Adaptive Backstepping Approach. *IEEE Trans. Ind. Electron.* **2019**, *66*, 5644–5652. [CrossRef]
22. Gao, Z.; Huang, Y.; Han, J. An alternative paradigm for control system design. In Proceedings of the 2001 American Control Conference, Arlington, VA, USA, 25–27 June 2001; Volume 4575, pp. 4578–4585.
23. Han, J. From PID to Active Disturbance Rejection Control. *IEEE Trans. Ind. Electron.* **2009**, *56*, 900–906. [CrossRef]
24. Qing, Z.; Gaol, L.Q.; Zhiqiang, G. On stability analysis of active disturbance rejection control for nonlinear time-varying plants with unknown dynamics. In Proceedings of the 2007 46th IEEE Conference on Decision and Control, New Orleans, LA, USA, 12–14 December 2007; pp. 3501–3506.
25. Gao, Z. Scaling and bandwidth-parameterization based controller tuning. In Proceedings of the 2003 Annual American Control Conference, Denver, CO, USA, 4–6 June 2003; pp. 4989–4996.

26. Zheng, Q.; Chen, Z.; Gao, Z. A practical approach to disturbance decoupling control. *Control. Eng. Pract.* **2009**, *17*, 1016–1025. [CrossRef]
27. Zhang, H.; Zhao, S.; Gao, Z.Q. An Active Disturbance Rejection Control Solution for the Two-Mass-Spring Benchmark Problem. In Proceedings of the 2016 American Control Conference, Boston, MA, USA, 6–8 June 2016; pp. 1566–1571.
28. Xu, B.; Zhou, J.; Xu, L. Adaptive Backstepping Control of Active Magnetic Bearings with Slice Rotor. *J. Vib. Eng. Technol.* **2022**, *10*, 795–808. [CrossRef]